ISA Transactions 160 (2025) 186–195

Contents lists available at ScienceDirect

ISA Transactions

journal homepage: www.elsevier.com/locate/isatrans

Research article

Sensorless Control of Permanent magnet in-wheel motor for EVs Using Global Fast Terminal Sliding Mode Observer

Hao Huang [a],*, Keqin Li [b], Chunfeng Yu [a], Zhonghua Sun [a], Yuanfeng Zhang [a], Zhibin Zhao [a], Bin Luo [a]

[a] Naval Aviation University Qingdao Campus, No. 2 , Siliu Middle Road, Qingdao, 210006, ShanDong, China
[b] Department of Computer Science State University of New York, Science Hall 249, New Paltz, 12561, New York, USA

ARTICLE INFO

Keywords:
Sensorless control
Permanent magnet in-wheel motor
Global fast sliding mode observer
Phase-lock loop

ABSTRACT

This article aims to provide a high-precision sensorless controller for permanent magnet in-wheel motors (PMIWMs) used in electric vehicles (EVs) when an unexpected failure of the position sensor occurs. To address this, we propose a position sensorless control method that combines a global fast terminal sliding mode observer (GFTSMO) with a phase-locked loop (PLL) estimation scheme. First, the GFTSMO is introduced to reduce the significant chattering that typically occurs in traditional sliding mode observers (SMO). This control scheme can help the state variable converge to an equilibrium state from any initial condition and minimize chattering. Second, we implement a PLL estimation scheme to replace the conventional arc-tangent estimation method. This method avoids the triggering of high-frequency oscillations, thereby improving the estimation precision and robustness of the control system. In addition, we discuss the stability of the proposed GFTSMO using the Lyapunov function. Simulation and tests on a motor platform demonstrate that the proposed position sensorless algorithm can track speed rapidly and accurately without overshooting. The proposed sensorless control can ensure the control stability of PMIWMs and can be applied in other occasions where installing motor sensors is challenging.

1. Introduction

In recent years, electric vehicles (EVs) powered by permanent magnet in-wheel motors (PMIWM) have become a significant focus of global research [1,2]. The use of PMIWM in EVs effectively addresses issues such as poor energy efficiency, slow response speeds, and environmental pollution associated with traditional vehicles [3,4]. While the PMIWM utilizes the permanent magnet synchronous motors (PMSMs) as its driving component and incorporates them within the wheels of electric vehicles, it necessitates a higher level of control demand in contrast to traditional PMSM. This increased demand for control arises from the absence of a transmission shaft and gearbox in EVs driven by PMIWM, which conduct to any speed change occurring in the PMIWM can cause an imbalance of EVs. Aiming at ensuring the balance and safety of EVs, it is crucial to ensure the high control precision and fast response speed of each PMIWM.

Regarding improving control precision and response speed, it is essential to implement real-time monitoring and feedback of speed and position signals, and the most widely used motor sensors are the resolver and photoelectric encoder. Considering the properties of these two sensors, the resolver exhibits inadequate control precision, which cannot apply to high-accuracy PMIWM control, and the photoelectric encoder cannot be applied to complex operational conditions such as dust, water vapor, and vibration due to its poor interference resistance [5,6]. Therefore, these two types of sensors cannot guarantee the stability and accuracy of feedback. In addition, installing mechanical sensors complicates the motor control system's layout and increases the unsprung mass of automobiles, which can deteriorate the EV performance [7,8]. Moreover, the installation of sensors can increase the cost of the EVs. Considering stability, EV performance, and cost, it is crucial to adopt the position and speed sensorless scheme for PMIWM.

To realize the position and speed sensorless scheme, a parameter adaptive algorithm for online parameters identification and feedback was proposed in [9], which can compensate for the nonlinearity of the inverter to eliminate control errors in estimation process. However, it is not suitable for heavy load occasions. To solve this, a sensorless motor drive scheme that combines hybrid observer for heavy-load position servo was designed in [10]. However, this method cannot ensure the estimation precision. To enhance the estimation precision of current and

* Corresponding author.
E-mail addresses: haohuang_130@whu.edu.cn (H. Huang), lik@nwpaltz.edu (K. Li), chunfen_qdxq@outlook.com (C. Yu), zhonghua_qdxq@outlook.com (Z. Sun), yuanfen_qdxq@outlook.com (Y. Zhang), zzbwoaiwojia@outlook.com (Z. Zhao), binluo_qdxq@outlook.com (B. Luo).

https://doi.org/10.1016/j.isatra.2025.02.022
Received 14 November 2024; Received in revised form 1 February 2025; Accepted 14 February 2025
Available online 1 March 2025

position, a sensorless machine drive scheme that combines predictive control of the motion model in the speed loop with phase current was considered in [11]. Additionally, a parameter-sensitive adaptive online decoupling sensorless control strategy was also proposed to improve the estimation accuracy of rotor position in [12]. In order to further reduce the estimation error, a flux estimation was proposed to calculate flux and reduce the indicating errors in [13]. In addition, a static error-free position estimation strategy was applied to eliminate DC errors and high-frequency noise in [14].

Compared with the methods mentioned above, the sliding mode observer (SMO) has become an ideal sensorless control scheme due to its advantages, such as the low requirement for modeling accuracy, insensitivity to parameter disturbances, simple control structure, and good robustness [15,16]. However, during the position sensorless control process of SMO, two key technical issues need to be overcome: Firstly, there is a chattering value of the conventional SMO during the control process, which can result in severe fluctuation of estimation process [17]. Secondly, the conventional SMO scheme adopts the traditional arc-tangent function algorithm to estimate the speed and position signal, which can trigger high-frequency oscillations and severely affect the accuracy of motor speed and position estimation [18].

The chattering phenomenon in control systems arises from the error that cannot approach zero within a finite time. To solve this issue, a composite super-twisting sliding mode control (STSMC) integrated with a novel disturbance observer was designed in [19]. This approach reduces the inevitable chattering phenomenon and estimates the lumped disturbance. However, it struggles to estimate the upper bound of this disturbance quickly. To further improve disturbance estimation, a finite-time adaptive STSMC was proposed in [20], which ensures that the dynamics of the tracking error can converge to zero in a finite time and boosts the estimation speed of lumped disturbance. In addition, a novel model-free STSMC method was developed in [21], enabling the state variables to converge rapidly to the reference value within a finite time and estimate unknown disturbances. Alongside STSMC, high-order sliding mode control (HOTSMC) can also facilitate the control error converge to zero. In [22], a high-order fast nonsingular terminal sliding mode control was introduced to enhance convergence speed and eliminate chattering. Furthermore, HOTSMC can be applied for harmonic suppression and disturbance compensation [23].

Compared with the STSMC and HOTSMC, global fast terminal sliding mode control (GFTSMC) has fewer control parameters and high-order sliding mode surfaces, which can make the control error converge to zero with less computational complexity of the control system, as well as save the cost of the PMIWM control system. As for the high-frequency oscillations of the arc-tangent function algorithm, the commonly solved method is adding a low-pass filter. However, this method can conduct the angle estimation error caused by the delay effect. The key idea to avoid high-frequency oscillations is to design a novel estimation scheme to replace the arc-tangent function.

In this paper, we design a global fast terminal sliding mode observer (GFTSMO) combined with a phase-loop lock (PLL) estimation algorithm. Firstly, a GFTSMO is designed for the control error of PMIWM to converge to zero in a finite time and reduce the chattering phenomenon. In addition, to further improve the position and speed estimation precision of the PMSM control, a PLL algorithm is designed to replace the arc-tangent position estimation algorithm, which can eliminate the high-frequency switching parts by integral function and enhance the estimation accuracy. The main contributions of this paper can be summarized as follows:

(1) A GFTSMO is proposed to replace SMO in this article to realize the estimation of the back electromotive force (BEF). This novel method can reduce the chattering value that occurred in the SMO and enable the tracking error to converge to zero in a finite time, which can further reduce the fluctuation of speed estimation.

(2) To achieve higher precision in feedback results, a PLL scheme is designed to estimate the system's position and speed signal. This method effectively prevents high-frequency vibrations in the system and reduces the error between the actual speed and the estimated speed.

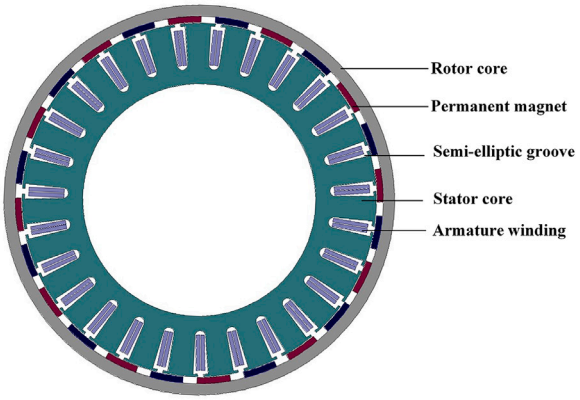

Fig. 1. The structure of PMIWM.

(3) Multiple sets of simulations and experiments designed to verify that the proposed sensorless controller based on the GFTSMO can achieve ideal sensorless control of the PMIWM, which owns a fast response speed and strong anti-interference ability. This controller demonstrates a rapid response time and robust anti-interference capability.

The whole paper is presented as follows: In Section 2, the PMIWM mathematical model is constructed; In Section 3, an observer based on the GFTSMO and a phase-lock loop(PLL) estimation scheme are designed; Section 4 verifies the proposed sensorless control strategy by simulation and physical platform test; Section 5 summarizes the whole paper.

2. Modeling of PMIWM

This paper takes the external rotor interior PMIWM as the research object and research on high-performance control strategies for PMIWM-driven vehicles under complex operating conditions. The motor structure is shown in Fig. 1, the number of stator slots is 27 and the rotor poles are 24, respectively, the axial length is 50 mm, and the built-in permanent magnet is located inside the rotor along the circumference. This motor provides high torque output for electric vehicles while reducing the consumption of permanent magnets. The dynamic equation of PMIWM is as follows

$$T_e - T_L = J\frac{d\omega}{dt} + B\omega \tag{1}$$

where T_e is electromagnetic torque, T_L is torque load, B is friction coefficient, ω is angular velocity, J is Moment of inertia. The torque of PMIWM can be given as

$$T_e = \frac{3}{2}P\left[\left(L_d - L_q\right)i_d i_q + \psi_f i_q\right] \tag{2}$$

where P is pole pairs, i_d and i_q are current of $d-q$ axis respectively, L_d and L_q are inductance of $d-q$ axis respectively, ψ_f is the magnetic flux. As the research object of this article is surface mounted motors, $L_d = L_q = L$, Eq. (2) can be simplified as

$$T_e = \frac{3}{2}P\psi_f i_q \tag{3}$$

The voltage in $\alpha-\beta$ stationary coordinate system can be expressed as

$$\begin{cases} u_\alpha = Ri_\alpha + L\frac{di_\alpha}{dt} + e_\alpha \\ u_\beta = Ri_\beta + L\frac{di_\beta}{dt} + e_\beta \end{cases} \tag{4}$$

Simplify (4) and the current of motor can be obtained as

$$\begin{cases} \frac{di_\alpha}{dt} = -\frac{R}{L}i_\alpha + \frac{1}{L}u_\alpha - \frac{1}{L}e_\alpha \\ \frac{di_\beta}{dt} = -\frac{R}{L}i_\beta + \frac{1}{L}u_\beta - \frac{1}{L}e_\beta \end{cases} \tag{5}$$

Back electromotive force can be expressed as follows

$$\begin{cases} e_\alpha = -\psi_f \omega \sin\theta \\ e_\beta = \psi_f \omega \cos\theta \end{cases} \tag{6}$$

where e_α and e_β are back electromotive force of $\alpha-\beta$ axis respectively, u_α and u_β are stator voltage of $\alpha-\beta$ axis respectively, i_α and i_β are stator current of $\alpha-\beta$ axis respectively, R is electronic winding reluctance, θ is the rotation angle of motor.

3. Global fast terminal sliding mode observer

In order to compensate for the chattering value and enhance convergence speed when approaching the convergence point in the traditional sliding surface [24,25], this section adopts a global fast terminal sliding surface, which can effectively combine the merits of linear and fast terminal sliding surface [26]. When the system state variable is distant from the equilibrium point, a linear sliding surface is implemented to enhance the state variable's convergence rate. Conversely, as the state variable approaches proximity to the equilibrium point, adopting a fast terminal sliding surface facilitates the system state variable's approach to the equilibrium state within a finite time frame. Introducing this sliding mode control surface can ensure a fast convergence speed when approaching the zero point and effectively suppress the problem of chattering value when approaching the equilibrium point, which can combine the characteristics of fast response speed and low estimation error.

3.1. Design of the traditional sliding mode controller

Establish the second-order nonlinear systems as

$$\begin{cases} \frac{dx_1}{dt} = x_2 \\ \frac{dx_2}{dt} = f(x) + d(t) + bu \end{cases} \tag{7}$$

where x_1 and c are state variables, b is a constant and $b > 0$, $f(x)$ is continuous function, $d(t)$ is external disturbances and $|d(t)| \le D$, b is a constant and $b > 0$, u is the output of the sliding mode controller.

Design the sliding mode surface based on the traditional sliding mode control(SMC) as

$$s = cx_1 + x_2 \tag{8}$$

Eq. (8) can be differentiated as

$$\frac{ds}{dt} = cx_2 + \frac{dx_2}{dt} \tag{9}$$

where s is the sliding mode surface, c is the control parameter of sliding mode surface.

Typically, the design of SMC can be categorized into two distinct phases: firstly, design the sliding mode reaching law of the control system; secondly, design the control input to direct the system trajectory towards the sliding mode surface, guaranteeing the fulfillment of the sliding mode reaching condition as determined by the Lyapunov function, as shown in (10).

$$\frac{dV}{dt} = s\frac{ds}{dt} \le 0 \tag{10}$$

Firstly, design the sliding mode reaching law proposed by Gao, as shown in (11)

$$\frac{ds}{dt} = -\varepsilon \mathrm{sgn}(s) \tag{11}$$

where ε and k are determined reaching parameters of the sliding mode controller, $\varepsilon > 0$, $k > 0$. Substitute (11) into (10) yields

$$\frac{dV}{dt} = s\frac{ds}{dt} = -\varepsilon \mathrm{sgn}(s)s = -\varepsilon|s| \le 0 \tag{12}$$

Secondly, design the SMC input $u(t)$ based on (11) and (7)

$$\begin{aligned} u(t) &= -\frac{1}{b}\left(f(x) + d(t) - \frac{dx_2}{dt}\right) \\ &= -\frac{1}{b}\left(f(x) + d(t) - \frac{ds}{dt} - cx_2\right) \\ &= -\frac{1}{b}\left(f(x) + d(t) + \varepsilon \mathrm{sgn}(s) - cx_2\right) \end{aligned} \tag{13}$$

By designing the sliding mode reaching law and control input, the control error can reach the equilibrium point, the sliding surface based on the SMO can be obtained as follows

$$s = cx_1 + \frac{dx_1}{dt} = 0 \tag{14}$$

Solve differential equation (14) yields

$$\int_0^t \frac{1}{x_1}\frac{dx_1}{dt}dt = \int_0^t -cdt \tag{15}$$

Solve (15) and the following equation can be obtained

$$\ln\frac{x_1(t)}{x_1(0)} = -ct \tag{16}$$

Based on (16), the convergence result can be obtained as

$$x_1(t) = e^{-ct}x_0(t) \tag{17}$$

From (17), we can obtain that when colored $t \to \infty$, the track error cannot converge to 0 in finite a time, which can deteriorate the control performance.

3.2. Design of the global fast terminal sliding mode controller

In order to make the tracking error converge to 0 within a finite time, the sliding surface based on the global fast terminal sliding mode control(GFTSMC) is designed as

$$s = x_2 + \alpha x_1 + \beta x_1^{q/p} \tag{18}$$

Eq. (18) can be differentiated as

$$\frac{ds}{dt} = \frac{dx_2}{dt} + \alpha x_2 + \frac{q\beta}{p}x_1^{\frac{q-p}{p}}x_2 \tag{19}$$

where α, β, p, q, are control parameters of global sliding surface, $p > q$, we denote $\alpha = 2$, $\beta = 1$, $p = 5, q = 3$ in this paper.

In order to meet the Lyapunov function $\frac{dV}{dt} = s\frac{ds}{dt} \le 0$, using the reaching law $\frac{ds}{dt} = -\varepsilon \mathrm{sgn}(s)$, which is shown in (11). Combine (7), (11) and (19), the control input of global fast terminal sliding mode surface can be obtained as

$$\begin{aligned} u(t) &= -\frac{1}{b}\left(f(x) + d(t) - \frac{dx_2}{dt}\right) \\ &= -\frac{1}{b}\left(f(x) + d(t) - (\frac{ds}{dt} - \alpha x_2 - \frac{q\beta}{p}x_1^{\frac{q-p}{p}}x_2)\right) \\ &-\frac{1}{b}(f(x) + d(t) + \varepsilon \mathrm{sgn}(s) + \alpha x_2 + \frac{q\beta}{p}x_1^{\frac{q-p}{p}}x_2) \end{aligned} \tag{20}$$

Through designing the sliding mode reaching law and control input, the state variable can reach the equilibrium point, and the sliding surface based on the GFTSMC can be expressed as

$$s = x_2 + \alpha x_1 + \beta x_1^{q/p} = 0 \tag{21}$$

Because $x_2 = \frac{dx_1}{dt}$, Eq. (21) can be expressed as follows

$$\frac{dx_1}{dt} + \alpha x_1 = -\beta x_1^{q/p} \tag{22}$$

Divide both sides of (22) by $x_1^{q/p}$ simultaneously yields

$$\frac{dx_1}{dt}x_1^{-q/p} + \alpha x_1^{(p-q)/p} = -\beta \tag{23}$$

Let $y = x_1^{(p-q)/p}$, $\frac{dy}{dt} = \frac{p-q}{p}\frac{dx_1}{dt}x_1^{-q/p}$, Eq. (23) can be simplified as follows

$$\frac{p}{p-q}\frac{dy}{dt} + \alpha y = -\beta \tag{24}$$

Multiply both sides of (24) by $\frac{p-q}{p}$ simultaneously yields

$$\frac{dy}{dt}+\frac{p-q}{p}\alpha y=-\frac{p-q}{p}\beta \tag{25}$$

Solve (25) and the following equation can be obtained

$$y=e^{-\int_0^t \frac{p-q}{p}\alpha dt}\left(\int_0^t -\frac{p-q}{p}\beta e^{\frac{p-q}{p}\alpha dt}+C\right) \tag{26}$$

When $x_1=0, y(0)=C$, Eq. (26) can be rewritten as

$$\begin{aligned} y&=e^{-\frac{p-q}{p}\alpha t}\left(\frac{p-q}{p}\beta\frac{p}{(p-q)\alpha}e^{\frac{p-q}{p}\alpha t}\Big|_0^t+y(0)\right)\\ &=-\frac{\beta}{\alpha}+\frac{\beta}{\alpha}e^{-\frac{p-q}{p}\alpha t}+y(0)e^{-\frac{p-q}{p}\alpha t}\end{aligned} \tag{27}$$

When $t=t_s$, the control can converge to the equilibrium state, $y=x_1{}^{(p-q)/p}=0$, Eq. (27) can be simplified as

$$\frac{\beta}{\alpha}e^{-\frac{p-q}{p}\alpha t_s}+y(0)e^{-\frac{p-q}{p}\alpha t_s}=\frac{\beta}{\alpha} \tag{28}$$

where $y(0)=x_1(0)^{\frac{p-q}{p}}$, the time t_s for convergence from any initial state to the equilibrium state can be expressed as

$$t_s=\frac{p}{\alpha(p-q)}\ln\frac{\alpha x_1(0)^{\frac{p-q}{p}}+\beta}{\beta} \tag{29}$$

From (29), we can validate that the control can reach the equilibrium state in infinite time t_s through setting the sliding mode control parameters α,β,p,q.

Based on (22), the following equation can be obtained

$$\frac{dx_1}{dt}=-\alpha x_1-\beta x_1^{q/p} \tag{30}$$

As the system state variable x_1 diverges from the origin, the convergence time is predominantly influenced by the fast terminal attractor ($\frac{dx_1}{dt}=-\beta x_1^{q/p}$). Conversely, as the system state variable x_1 nears equilibrium, the convergence time is chiefly determined by ($\frac{dx_1}{dt}=-\alpha x_1$), accompanied by an exponential decay of x_1. Therefore, by introducing a global terminal sliding surface, the system state variables can converge within a finite time while retaining the fast performance of the linear sliding surface in approaching the equilibrium state.

Fig. 2 provides a comparative analysis of the performance of the GFTSMC and SMC methodologies. In Fig. 2(a), the phase trajectory of the system state emanating from the initial position under the influence of these two sliding mode surfaces is depicted, indicating that GFTSMC achieves a more rapid convergence rate than SMC. Fig. 2(b) presents the convergence process of the system state concerning these sliding mode surfaces, highlighting that GFTSMC exhibits a reduced steady-state error compared to SMC. In Fig. 2(c), the control input u is demonstrated, revealing that GFTSMC produces smoother control inputs with minimal chattering relative to SMC. Fig. 2(d) presents the position tracking curves corresponding to these sliding mode surfaces, illustrating that GFTSMC attains higher speed and reduced error when aligning with the reference position signal. In summary, GFTSMC demonstrates enhanced performance in terms of convergence speed, steady-state error, and chattering suppression compared to SMC.

3.3. State variable of global fast terminal sliding mode surface

Construct the PMIWM current equation as follows

$$\frac{di_s}{dt}=-\frac{R}{L}i_s+\frac{1}{L}u_s-\frac{1}{L}e_s \tag{31}$$

where $i_s=\left[i_\alpha,i_\beta\right]^T$, $u_s=\left[u_\alpha,u_\beta\right]^T$, $e_s=\left[e_\alpha,e_\beta\right]^T$, construct the PMIWM sliding mode observer equation as

$$\frac{d\hat{i}_s}{dt}=-\frac{R}{L}\hat{i}_s+\frac{1}{L}u_s-\frac{1}{L}U_s \tag{32}$$

where $\hat{i}_s$ is the observe value of i_s, U_s is the control output and $U_s=\left[U_\alpha,U_\beta\right]^T$.

Subtract (31) from (32) yields

$$\frac{d\tilde{i}_s}{dt}=-\frac{R}{L}\tilde{i}_s+\frac{1}{L}e_s-\frac{1}{L}U_s \tag{33}$$

Define the PMIWM state variables x_1 and x_2 as follows

$$\begin{cases} x_1=\tilde{i}_s=\hat{i}_s-i_s\\ x_2=\frac{d\tilde{i}}{dt}=-\frac{R}{L}\tilde{i}_s+\frac{1}{L}e_s-\frac{1}{L}U_s\end{cases} \tag{34}$$

3.4. Control input of global fast terminal sliding mode observer

Construct the Lyapunov function as follows

$$V=\frac{1}{2}s^2 \tag{35}$$

The stability criteria for Lyapunov functions is as follows

$$\frac{dV}{dt}=s\frac{ds}{dt}\le 0 \tag{36}$$

Substitute (19) into (36)

$$\begin{aligned}\frac{dV}{dt}&=s\left(\frac{dx_2}{dt}+\alpha x_2+\frac{q\beta}{p}x_1^{\frac{q-p}{p}}x_2\right)\\ &=s\left(\frac{q\beta}{p}\tilde{i}_s^{\frac{q-p}{p}}\frac{d\tilde{i}_s}{dt}+\alpha\frac{d\tilde{i}_s}{dt}+\frac{d^2\tilde{i}_s}{dt^2}\right)\\ &=s\left(\left(\frac{q\beta}{p}\tilde{i}_s^{\frac{q-p}{p}}+\alpha\right)\frac{d\tilde{i}_s}{dt}+\frac{d^2\tilde{i}_s}{dt^2}\right)\\ &=sF\left(\frac{d\tilde{i}_s}{dt}+\frac{1}{F}\frac{d^2\tilde{i}_s}{dt^2}\right)\end{aligned} \tag{37}$$

where $V=\left[V_\alpha,V_\beta\right]^T$, $s=\left[s_\alpha,s_\beta\right]^T$, $F=\frac{q\beta}{p}\tilde{i}_s^{\frac{q-p}{p}}+\alpha>0$, Decompose (37) into the $\alpha-\beta$ axis of PMIWM

$$\begin{cases}\frac{dV_\alpha}{dt}=s_\alpha F\left(\frac{d\tilde{i}_\alpha}{dt}-\frac{1}{FL}\left(R\frac{d\tilde{i}_\alpha}{dt}-\frac{de_\alpha}{dt}+\frac{dU_\alpha}{dt}\right)\right)\\ \frac{dV_\beta}{dt}=s_\beta F\left(\frac{d\tilde{i}_\beta}{dt}-\frac{1}{FL}\left(R\frac{d\tilde{i}_\beta}{dt}-\frac{de_\beta}{dt}+\frac{dU_\beta}{dt}\right)\right)\end{cases} \tag{38}$$

In order to satisfy the Lyapunov equation, the control input based on global fast terminal sliding surface is designed as

$$\begin{cases}U_\alpha=\int_0^t\left(\left(D+\eta\right)\mathrm{sgn}(s_\alpha)-\left(R\frac{di_\alpha}{dt}-FL\frac{di_\alpha}{dt}\right)\right)d\tau\\ U_\beta=\int_0^t\left(\left(D+\eta\right)\mathrm{sgn}(s_\beta)-\left(R\frac{di_\beta}{dt}-FL\frac{di_\beta}{dt}\right)\right)d\tau\end{cases} \tag{39}$$

By substituting (39) into (38), it can be obtained as

$$\begin{cases}\frac{dV_\alpha}{dt}=S_\alpha F\left(\frac{d\tilde{i}_\alpha}{dt}-\frac{1}{FL}\left(\begin{array}{c}R\frac{d\tilde{i}_\alpha}{dt}-\frac{de_\alpha}{dt}+(D+\eta)\\ \mathrm{sgn}\left(S_\alpha\right)-\left(R\frac{d\tilde{i}_\alpha}{dt}-FL\frac{d\tilde{\tau}_\alpha}{dt}\right)\end{array}\right)\right)\\ =-S_\alpha\frac{1}{L}\left((D+\eta)\mathrm{sgn}\left(S_\alpha\right)-\frac{de_\alpha}{dt}\right)\\ \frac{dV_\beta}{dt}=S_\beta F\left(\frac{d\tilde{i}_\beta}{dt}-\frac{1}{FL}\left(\begin{array}{c}R\frac{d\tilde{i}_\beta}{dt}-\frac{de_\beta}{dt}+(D+\eta)\\ \mathrm{sgn}\left(S_\beta\right)-\left(R\frac{d\tilde{i}_\beta}{dt}-FL\frac{d\tilde{c}_\beta}{dt}\right)\\ =-S_\beta\frac{1}{L}\left((D+\eta)\mathrm{sgn}\left(S_\beta\right)-\frac{de_\alpha}{dt}\right)\end{array}\right)\right)\end{cases} \tag{40}$$

When Eq. (40) meets $D>\max(\left|\frac{de_\alpha}{dt}\right|,\left|\frac{de_\beta}{dt}\right|)$, the following conclusion can be obtained

$$\begin{cases}\frac{dV_\alpha}{dt}\le-\frac{1}{L}s_\alpha\mathrm{sgn}(s_\alpha)\le 0\\ \frac{dV_\beta}{dt}\le-\frac{1}{L}s_\beta\mathrm{sgn}(s_\beta)\le 0\end{cases} \tag{41}$$

To maintain the stability of the control system under the proposed GFTSMO, the control parameter D is designed as

$$D=k\max(\left|\frac{de_\alpha}{dt}\right|,\left|\frac{de_\beta}{dt}\right|) \tag{42}$$

In Eq. (42), the control parameter k must satisfy $k>1$ to meet the Lyapunov function, which ensures the global fast terminal sliding surface can reach 0 in a finite time. At this point, Eq. (18) satisfies

$$s=x_2+\alpha x_1+\beta x_1^{q/p}=0 \tag{43}$$

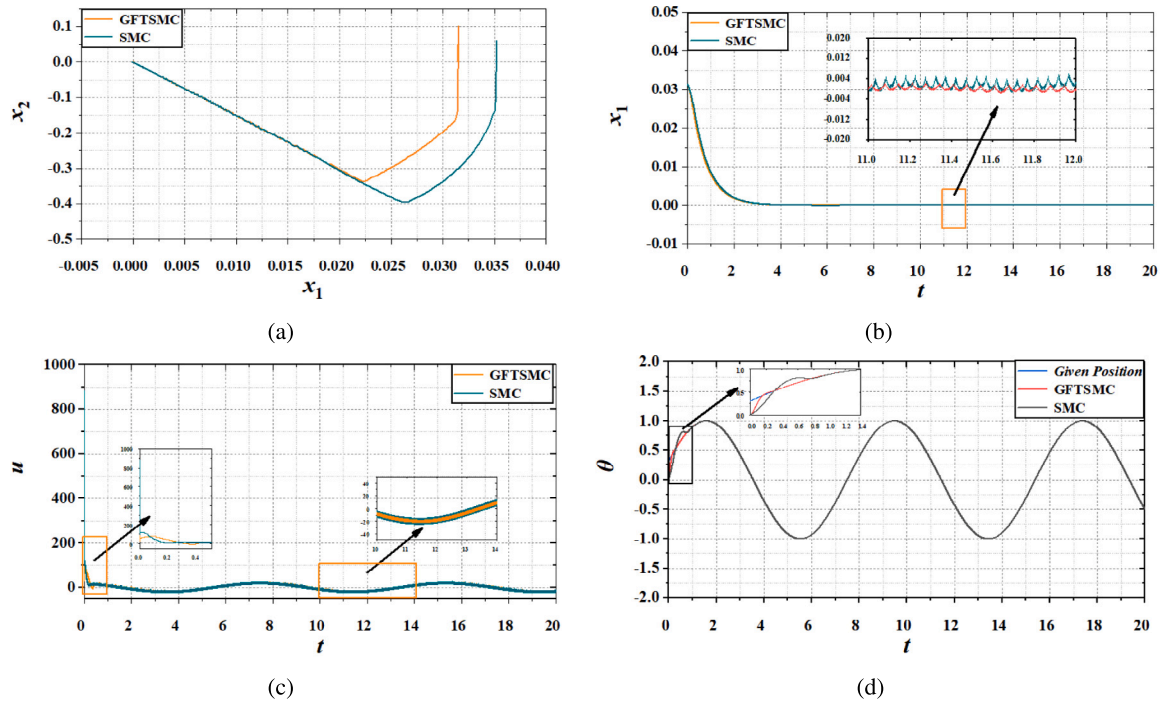

Fig. 2. Performance comparison between GFTSMC and SMC (a) Phase trajectory (b) System state convergence (c) Control input (d) Position tracking.

When the state variable can converge to 0 in a finite time, $\tilde{i}_s = \frac{d\tilde{i}}{dt} = 0$. Eq. (33) can be simplified as

$$-\frac{R}{L}\tilde{i}_s + \frac{1}{L}e_s - \frac{1}{L}U_s = 0 \tag{44}$$

When $\tilde{i}_s = 0$, simplify (44) as follows

$$e_s = U_s \tag{45}$$

U_s can be obtained from (39), so the back electromotive force e_s can be obtained based on the control input U_s.

Compared with the GFTSMO, the conventional SMO has a non-continuous sign function in the current estimation error, which can cause chattering and affect the control accuracy. However, the sign function under the GFTSMO can be suppressed through integral filtering. In addition, there is no need for a low-pass filter to reduce the discontinuous high-frequency switching signals with the GFTSMO, which can avoid phase delay caused by filtering back electromotive force estimation during the control process. In addition, this proposed GFTSMO scheme can be applied to other consensus control problems, such as resilient leaderless and leader–follower, multi-object consensus control issues [27,28].

3.5. Rotor position estimation based on PLL

Based on the BEF signal observed by GFTSMO, the position signal can be estimated, and the commonly used estimation method is arc-tangent function, which can be expressed as

$$\hat{\theta} = -\arctan\frac{e_\alpha}{e_\beta} = -\arctan\frac{U_\alpha}{U_\beta} \tag{46}$$

From (39) and (46), there is a switching function $\mathrm{sgn}(s_\alpha)$ and $\mathrm{sgn}(s_\beta)$ in U_α and U_β, which can trigger high-frequency oscillations [29,30], resulting in significant errors in the estimation process, we adopt a phase-locked loop (PLL)To solve this issue. The velocity position estimation block diagram is shown in Fig. 3.

Denote $|e| = \sqrt{{e_\alpha}^2 + {e_\beta}^2}$, then e_α and e_β can be expressed as

$$\begin{cases} e_\alpha = |e|\sin\theta \\ e_\beta = |e|\cos\theta \end{cases} \tag{47}$$

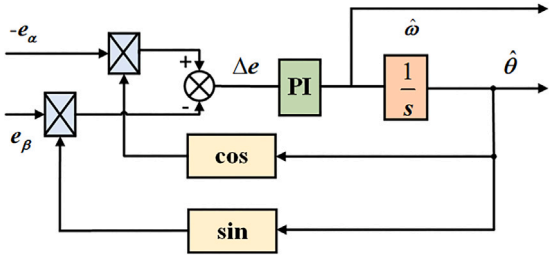

Fig. 3. Phase-locked loop estimation.

According to Fig. 3, the following equation can be obtained

$$\begin{aligned} \Delta e &= -e_\alpha\cos\hat{\theta} - e_\beta\sin\hat{\theta} \\ &= -|e|\sin\theta\cos\hat{\theta} + |e|\cos\theta\sin\hat{\theta} \\ &= -|e|\sin\theta\cos(\theta+\tilde{\theta}) + |e|\cos\theta\sin(\theta+\tilde{\theta}) \\ &= -|e|\sin\theta(\cos\theta\cos\tilde{\theta} - \sin\theta\sin\tilde{\theta}) + |e|\cos\theta(\sin\theta\cos\tilde{\theta} + \cos\theta\sin\tilde{\theta}) \\ &= |e|\sin\theta\sin\theta\sin\tilde{\theta} + |e|\cos\theta\cos\theta\sin\tilde{\theta} \\ &= |e|\sin\tilde{\theta} \end{aligned} \tag{48}$$

where $\tilde{\theta}$ represents the error between $\hat{\theta}$ and θ and $\tilde{\theta} = \hat{\theta} - \theta$. When $|\tilde{\theta}| = \left|\hat{\theta} - \theta\right| \le \frac{\pi}{6}$ is satisfied, $\sin\tilde{\theta} \approx \tilde{\theta}$, Eq. (48) can be simplified as

$$\Delta e = |e|\sin\tilde{\theta} \approx |e|\,\tilde{\theta} \tag{49}$$

From (49), it can conclude that the control input Δe of PI controller in Fig. 3 is proportional to $\tilde{\theta}$, and The PI controller can smooth the high-frequency switching term of Δe through the integral controller.

Based on the above methods, the GFTSMO and PLL velocity position estimation(abbreviated as GFTSMO-PLL) are shown in Fig. 4, and the estimation method is executed as follows:

Step 1: Estimate the current of PMIWM through GFTSMO and subtract the estimated current signal from the detected actual current to obtain the current estimation error.

Step 2: Construct a GFTSMO based on this current estimation error and obtain the estimated BEF through the design of the GFTSMO

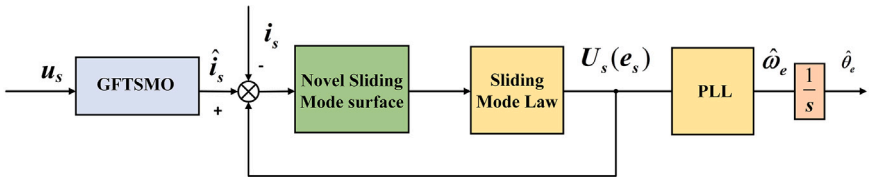

Fig. 4. The GFTSMO and PLL velocity position estimation.

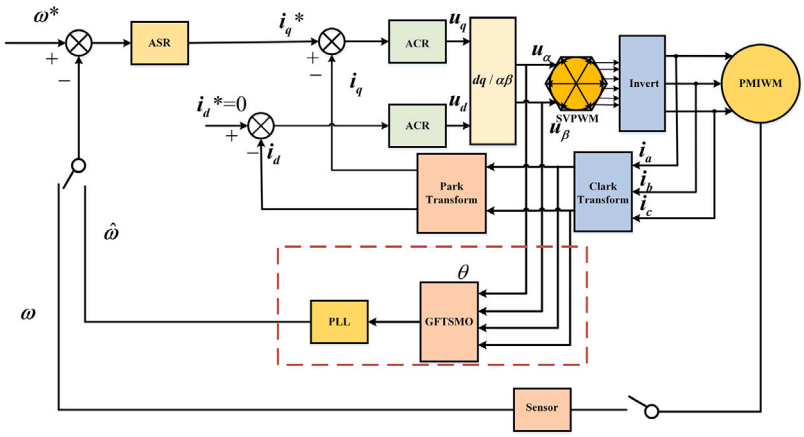

Fig. 5. PMIWM sensorless control system.

control law.

Step 3: Estimate the position and speed signal of the PMIWM through using the PLL estimation strategy.

4. Simulation and experiments

This section establishes the PMIWM position sensorless control system, as shown in Fig. 5. In this control system, the sliding mode algorithm mentioned in [31] is adopted to control both the speed and current control loops. Regarding acquiring speed and position signals, we can choose between sensor control and sensorless control strategies by switching on or off. Data from the traditional position sensor is the reference value and data from the sensorless control scheme is the observed value. To validate the observer precision, the proposed sensorless control strategy was compared with the sliding mode observer based on arctangent function rotor position estimation (SMO-Atan) and the global fast terminal observer algorithm based on arc-tangent function rotor position estimation (GFTSMO-Atan) through Matlab/Simulink simulation tests.

4.1. Sensorless control simulation test

This section conducts simulation tests in PMIWM to compare the observed performance of current and BEF from the proposed GFTSMO and conventional SMO. The observed values are presented in Figs. 6 and 7. The observed values of the BEF are also shown in Figs. 7 and 8, respectively.

Fig. 6(a) and (b) represent the observed value of i_α of PMIWM under GFTSMO and conventional SMO schemes, respectively. As shown in Fig. 6(a), because the proposed GFTSMO adopts a nonlinear surface, which can help suppress the chattering value during the convergence process through integral filtering, the simulation result presents a minor error between the observed value and the actual output value. There is almost no current fluctuation during the observation process. Compared to the GFTSMO scheme, the conventional SMO control scheme in Fig. 6(b) has more significant current fluctuations and poorer tracking performance, which owes to the switching function sgn(x) can conduct to severe chattering value during the control process.

Table 1
Comparison of estimation performance of observers.

Symbol	GFTSMO	SMO
Maximum estimation error of i_α (A)	1.83	4.86
Maximum estimation error of i_β (A)	2.01	5.64
Maximum estimation fluctuation of e_α (V)	3.95	21.5
Maximum estimation fluctuation of e_β (V)	3.87	22.3

Fig. 7(a) and (b) represent the observed value of i_β, which owes the similar amplitude and frequency of i_α, with only a phase difference. Compared to the estimation of Fig. 7(a) and (b), the observation scheme based on the proposed GFTSMO scheme shows the ideal performance of the β Axis current observation within slight current fluctuation, which is mainly attributed to GFTSMO's ability to reduce the control chattering.

Figs. 8 and 9 show the simulation estimation tests of BEF e_α and e_β under the GFTSMO and conventional SMO schemes, respectively. From Figs. 8(a) and 9(a), we can find that the proposed GFTSMO estimation strategy provides a relatively smooth simulation curve when estimating the BEF value, and the estimated fluctuations of e_α and e_β are within 4 V. The BEF estimation results under the conventional SMO estimation strategy shown in Figs. 8(b) and 9(b) fluctuate significantly, mainly due to the chattering phenomenon in conventional SMO.

Comparing the simulation tests of current and back electromotive force estimation in PMIWM using GFTSMO and conventional SMO in Figs. 6, 7, 8, and 9, the GFTSMO proposed in this article has more minor fluctuations compared to traditional SMO, mainly because GFTSMO can approach the error to zero, as shown in Eq. (29), which can reduce the chattering value and improve the control accuracy of sliding mode observation. Based on the above advantages, PMIWM can accurately estimate position and speed information during sensorless control driving, improving the control performance of PMIWM. The comparison of estimation performance data between the two observers is shown in Table 1.

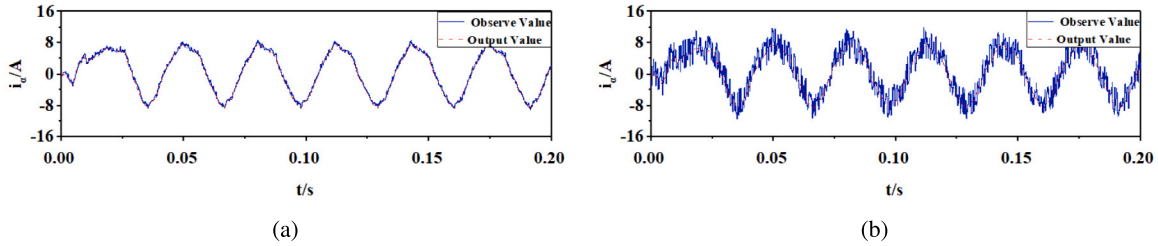

Fig. 6. Estimation simulation of i_α (a) GFTSMO (b) SMO.

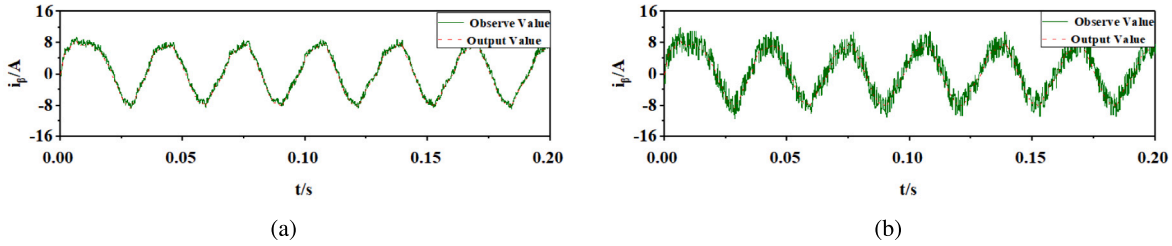

Fig. 7. Estimation simulation of i_β (a) GFTSMO (b) SMO.

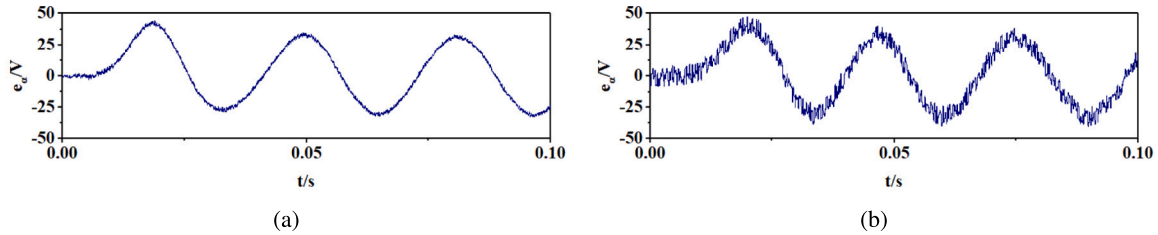

Fig. 8. Estimation simulation of e_α (a) GFTSMO (b) SMO.

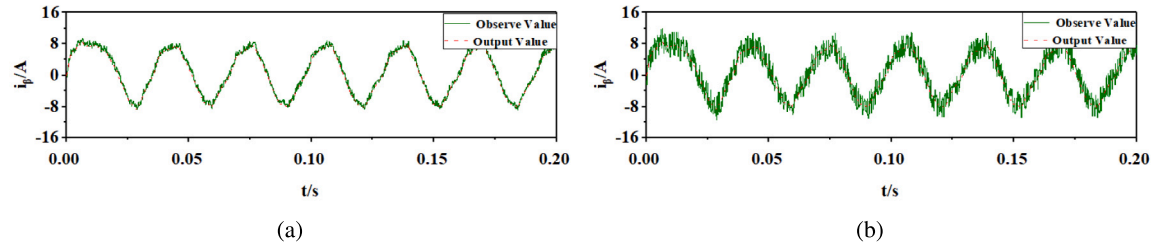

Fig. 9. Estimation simulation of e_β (a) GFTSMO (b) SMO.

4.2. Sensorless control experimental test

Based on the above simulation tests, the PMIWM sensorless control technology designed in this paper based on GFTSMO has precise back electromotive force and current estimation performance. This section will present experimental tests on the motor physical platform based on Links-RT to demonstrate the sensorless control strategy's control effect on the motor test platform. The motor platform and its control structure are shown in Fig. 10.

The motor experimental testing platform is established based on the Links-RT simulation system and consists of a motor towing platform (load motor, torque sensor, drive motor), an oscilloscope, a drive controller, and a PC. The parameters of the motor and the physical platform components are shown in Tables 2 and 3, respectively.

Fig. 11 shows the experimental results when receiving a starting command of 1000 r/min under three sensorless control strategies: GFTSMO based on PLL position estimation(GFTSMO-PLL), GFTSMO based on arctangent position estimation(GFTSMO-Atan), and SMO based on the arctangent position estimation(SMO-Atan). By comparing Fig. 11(a)–(c), the proposed sensorless control technology based on GFTSMO-PLL has a fast starting response speed, which can complete the starting response within 75 ms. It has a small tracking error during the response process. Compared with the GFTSMO-PLL control

Table 2
Motor parameters.

Symbol	Name	Value
B	Viscous friction coefficient	0.008 N m s
L_q	q-axis stator inductance	10.0 mH
L_d	d-axis stator inductance	10.0 mH
J	Moment of inertia	0.004 kg m^2
ψ	Rotor flux linkage	0.285 Wb
R	Resistance	2.375 Ω
P	Pole pair	4
T_s	Sample time	0.01 m s
f	Switching frequency	8 kHz

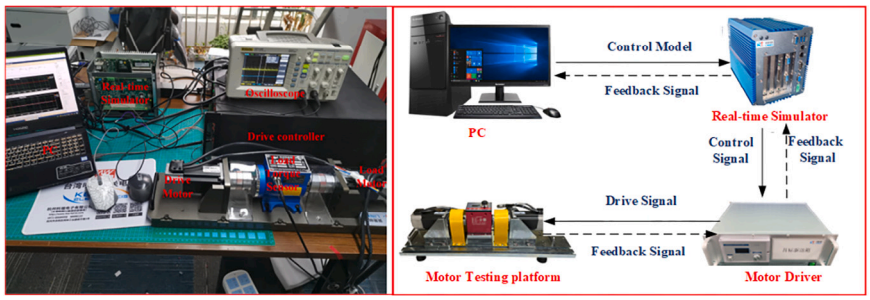

Fig. 10. Motor experimental testing platform.

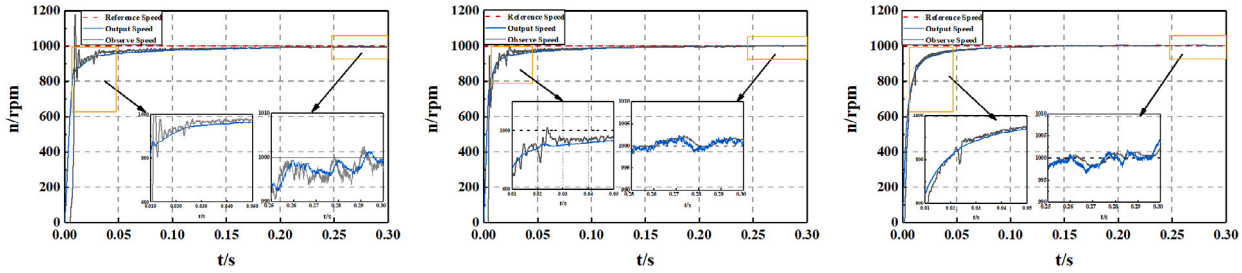

Fig. 11. Experimental test of starting (1000r/min) (a) SMO-Atan (b) GFTSMO-Atan (c) GFTSMO-PLL.

Table 3
Platform components.

Components	Name	Manufacturer/Location
Collection card	Links-IPC-DAQ-04	Links/China
PMIWM	PMIWM-01	Links/China
Load sensor	POB1KAO	Kilster/German
Control box	Links-Box-03	Links/China
Control software	RT-Sim Plu	Links/China

Table 4
Comparison of starting performance of PMIWM.

Symbol	SMO-Atan	GFTSMO-Atan	GFTSMO-PLL
Start response time (1000 r/min) (s)	0.243	0.157	0.128
Maximum tracking error (startup) (r/min)	283.6	62.4	18.7
Maximum tracking error (stable) (r/min)	8.4	4.6	3.8

strategy, the other two sensorless control strategies have defects in the observed accuracy and position velocity extraction strategy, resulting in overshoot and significant tracking errors during the starting process. The detailed comparison of starting performance is shown in Table 4.

In order to validate the acceleration ability of the proposed scheme, we conduct acceleration experiments. Fig. 12(a)–(c) show the speed observation and d-axis current results of PMIWM under these three control strategies, respectively. Comparing Fig. 12(a)–(c), the GFTSMO-PLL control scheme can accelerate without overshoot value, showing better acceleration performance than the other control strategies. In addition, during the acceleration process, the fluctuation of current i_d is minor under the GFTSMO-PLL control scheme. The detailed comparison of acceleration performance is shown in Table 5.

In order to validate the anti-disturbance ability of the proposed GFTSMO strategy, we conduct loading and unloading experiments based on the motor's physical platform. Fig. 13(a)–(c) show the speed observation and torque detection results of PMIWM under these three control strategies, respectively.

According to Fig. 13(c), the PMIWM can receive less fluctuation in speed regulation under the sensorless control of GFTSMO-PLL when receiving external load interference, which can be controlled within 45 r/min, and the tracking error during the control process can be limited within 10 r/min. Compared with the GFTSMO-PLL scheme, the motor's anti-interference ability is significantly weakened under sensorless control based on GFTSMO-Atan. The speed fluctuation amplitude of the output value exceeds twice that of the GFTSMO-PLL strategy, as presented in Fig. 13(b). The sensorless control strategy based on SMO-Atan exhibits significant amplitude fluctuations and overshoot in the output and observation values when receiving load disturbances, with the maximum fluctuation of the output value exceeding 90 r/min. By comparing the above load experimental results, the proposed GFTSMO-PLL sensorless control strategy has good speed regulation performance, strong anti-interference ability, and good robustness, which can effectively ensure the stability of distributed PMIWM driving under load disturbances. Table 6 shows a detailed comparison of loading performance.

In order to demonstrate the performance of position estimation based on the proposed GFTSMO-PLL strategy, a rotor position estimation experiment was conducted at a command of 500 r/min. The actual output value of the rotor position was detected through a 2500-line photoelectric encoder and compared with the position observation value. Fig. 13 presents the position estimation testing under three control strategies under the instruction speed of 600 r/min.

Comparing the experimental results 14(a)–(c) of PMIWM rotor position estimation under the three strategies, we can find tracking error of the proposed GFTSMO-PLL sensorless control strategy proposed in this paper can be controlled within 0.25 rad, reflecting good rotor position estimation accuracy and stability. Compared to the GFTSMO-PLL scheme, the tracking accuracy of the other two control strategies needs to be improved. As for the GFTSMO-Atan sensorless control strategy, there is an 8% amplitude fluctuation during the steady state. The SMO-Atan scheme has a tracking error over 0.4 rad during position estimation, and the amplitude fluctuation exceeds 10%.

5. Conclusion

In this paper, we design a global fast terminal sliding mode observer (GFTSMO) combined with a phase-loop lock (PLL) estimation algorithm. Firstly, a GFTSMO-based strategy is used to research the position

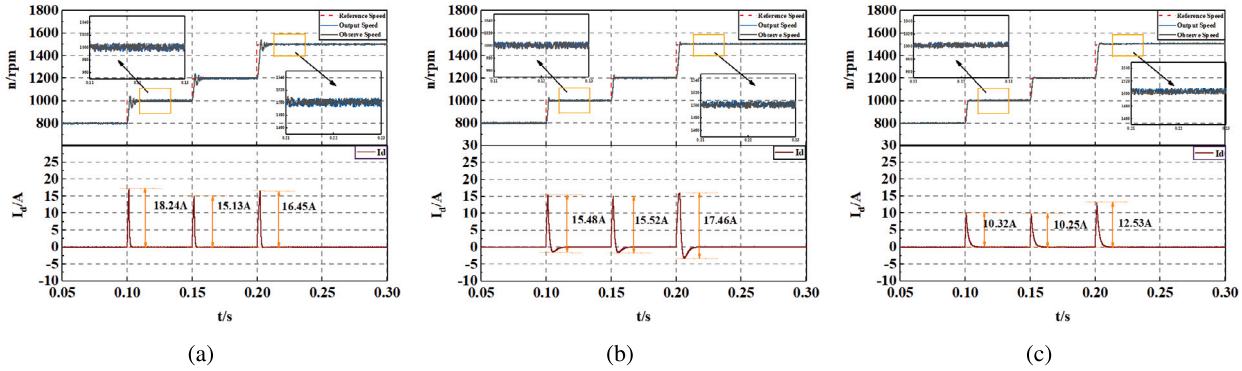

Fig. 12. Experimental test of acceleration (a) SMO-Atan (b) GFTSMO-Atan (c) GFTSMO-PLL.

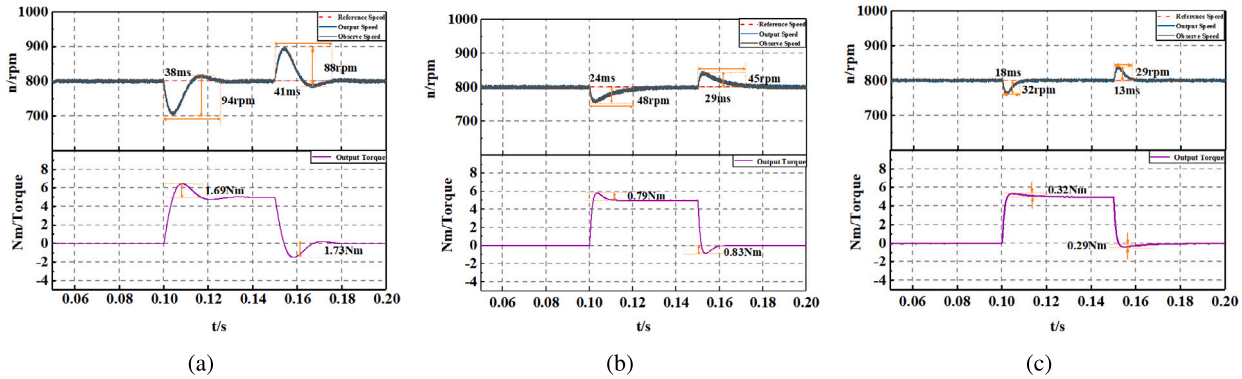

Fig. 13. Experimental test of loading (a) SMO-Atan (b) GFTSMO-Atan (c) GFTSMO-PLL.

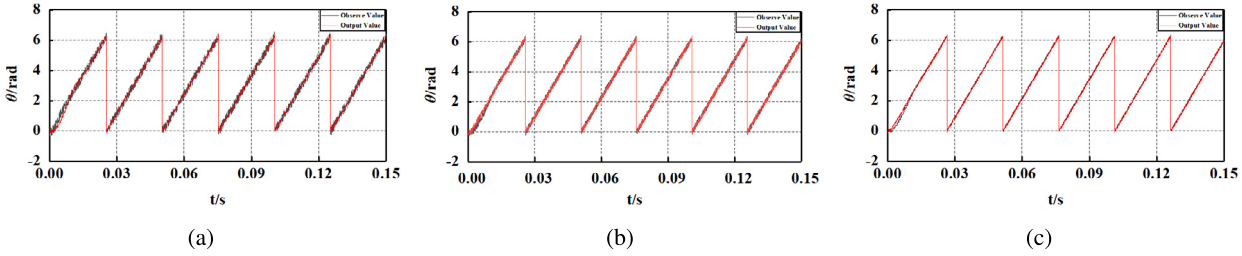

Fig. 14. Experimental test of position estimation (a) SMO-Atan (b) GFTSMO-Atan (c) GFTSMO-PLL.

Table 5
Comparison of acceleration performance of PMIWM.

Symbol	SMO-Atan	GFTSMO-Atan	GFTSMO-PLL
Average acceleration response time (observed value) (s)	0.027	0.025	0.013
Average acceleration response time (output value) (s)	0.028	0.024	0.012
Maximum acceleration response overshoot (r/min)	43.2	25.8	0
Maximum acceleration current fluctuation (A)	18.24	17.46	12.53

Table 6
Comparison of loading performance of PMIWM.

Symbol	SMO-Atan	GFTSMO-Atan	GFTSMO-PLL
Loading response time (observed value) (s)	0.038	0.023	0.018
Loading response time (output value) (s)	0.041	0.024	0.016
Loading response speed fluctuation (observed value) (r/min)	94.2	48.5	32.7
Loading response speed fluctuation (output value) (r/min)	93.8	47.3	32.3
Unloading response time (observed value) (s)	0.042	0.030	0.013
Unloading response time (output value) (s)	0.045	0.029	0.012
Unloading response speed fluctuation (observed value) (r/min)	88.3	46.6	29.3
Unloading response speed fluctuation (output value) (r/min)	87.6	45.3	28.5

sensorless control of the PMIWM system. Compared to the conventional SMO, the proposed method reduces the high-frequency chattering value and enables the state variable convergence to reach zero. Through the observation result, the proposed GFTSMO can eliminate about 80% BEF fluctuation and 64% current fluctuation, reducing the chattering value without sacrificing the converging value. In addition, a PLL estimation strategy is proposed to obtain a more precise speed and position signal, limiting the angle estimation error of the motor to within 0.25 rad and enhancing the anti-interference ability. This GFTSMO-PLL-based sensorless control can be adopted for EVs, small aircraft, robots, et al. In addition, the control parameters of the GFTSMO are constant, which cannot be adjusted to obtain the ideal control performance. Our future work will be dedicated to automatic parameter adjustment of PMIWM to obtain better control performance.

CRediT authorship contribution statement

Hao Huang: Conceptualization. **Keqin Li:** Formal analysis. **Chunfeng Yu:** Funding acquisition. **Zhonghua Sun:** Resources. **Yuanfeng Zhang:** Project administration. **Zhibin Zhao:** Software. **Bin Luo:** Methodology.

Declaration of competing interest

The authors declare that they have no known competing financial interests or personal relationships that could have appeared to influence the work reported in this paper.

Acknowledgments

This work was supported by National Key Research and Development Plan (2016YFC0802903) and National Natural Science Foundation of China under Grant Number (61671470).

References

[1] Zhang Sai, Shen An-wen, Luo Xin, Qi-peng Tang, Li Zi-cheng. Multi-sliding mode current disturbance suppression scheme based model reference adaptive system for sensorless control of permanent magnet synchronous motor. ISA Trans 2023;137:615–28.

[2] Lacombe Rémi, Gros Sébastien, Murgovski Nikolce, Kulcsár Balázs. Distributed eco-driving control of a platoon of electric vehicles through riccati recursion. IEEE Trans Intell Transp Syst 2023;24(3):3048–63.

[3] Ren Jun-Jie, Liu Yan-Cheng, Wang Ning, Liu Si-Yuan. Sensorless control of ship propulsion interior permanent magnet synchronous motor based on a new sliding mode observer. ISA Trans 2015;54:15–26.

[4] Liu Cong, Liu Hui, Han Li-jin, Wang Wei-da, Guo Cong-shuai. Multi-level coordinated yaw stability control based on sliding mode predictive control for distributed drive electric vehicles under extreme conditions. IEEE Trans Veh Technol 2023;72(1):280–96.

[5] Liu Shao-bo, Wang Qi-wei, Zhang Guo-qiang, Wang Gao-lin, Xu Dian-guo. Online temperature identification strategy for position sensorless PMSM drives with position error adaptive compensation. IEEE Trans Power Electron 2022;37(7):8502–12.

[6] Pathak Pawan Kumar, Yadav Anil Kumar, Padmanaban Sanjeevikumar, Twala Bhekisipho, Kamwa Innocent. Design of smart battery charging circuit via photovoltaic for hybrid electric vehicle. IET Renew Power Gener 2023;Early Access.

[7] Lin Xin-po, Zhang Bo, Fang Shu-xian, Xu Rui-qi, Guo Shi-chang, Liu Jian-xing. Adaptive generalized super twisting sliding mode control for PMSMs with filtered high-gain observer. ISA Trans 2023;138:639–49.

[8] Pathak Pawan Kumar, Yadav Anil Kumar, Padmanaban Sanjeevikumar, Alvi PA. Design of robust multi-rating battery charger for charging station of electric vehicles via solar PV system. Electr Power Compon Syst 2022;50(14–15):751–61.

[9] Chen Jia-hao, Mei Jie, Yuan Xin, Zuo Yue-fei, Zhu Jing-wei, Lee Christopher HT. Online adaptation of two-parameter inverter model in sensorless motor drives. IEEE Trans Ind Electron 2022;69(10):9860–71.

[10] Qian Lin-fang, Sun Le, Wang Kuan, Tong Ming-hao. Fusion of position estimation techniques for a swing servo by a permanent-magnet synchronous machine. IEEE Trans Ind Electron 2023;70(7):6551–62.

[11] Sun Le, Li Xiao-xiang, Chen Long-miao. Motor speed control with convex optimization-based position estimation in the current loop. IEEE Trans Power Electron 2021;36(9):10906–19.

[12] Zhu Xiao-yong, Zhang Li, Xiao Xiang-hua, Lee Christopher HT, Que Hong-jie. Adjustable-flux permanent magnet synchronous motor sensorless drive system based on parameter-sensitive adaptive online decoupling control strategy. IEEE Trans Transp Electrification 2023;9(1):501–11.

[13] Chen Jia-hao, Yang Guang-hui, Yuan Xin, Zhu Jing-wei, Hu Yi-hua, Lee Christopher HT. Experimental validation of a minimum-order sensorless induction motor control method. IEEE J Emerg Sel Top Power Electron 2024;12(4):3715–28.

[14] Yu Yan-jun, Shao Yan-zhen, Chai Feng, Cui Ming-kai. Static-errorless position estimation for sensorless PMSM drives with enhanced robustness against the full-frequency domain disturbance. IEEE Trans Power Electron 2022;37(5):5884–97.

[15] Bosso Alessandro, Tilli Andrea, Conficoni Christian. A hybrid sensorless observer for the robust global asymptotic flux reconstruction of permanent magnet synchronous machines. IEEE Control Syst Lett 2022;6:3367–72.

[16] Liu Tian-yi, Zhu ZQ, Wu Xi-meng, Wu Zhan-yuan, Stone David A, Foster Martin P. A position error correction method for sensorless control of dual three-phase permanent magnet synchronous machines. IEEE Trans Ind Appl 2022;58(3):3589–601.

[17] Dong Shan-ling, Liu Mei-qin, Wu Zheng-Guang, Shi Kai-bo. Observer-based sliding mode control for Markov jump systems with actuator failures and asynchronous modes. IEEE Trans Circuits Syst II: Express Briefs 2021;68(6):1967–71.

[18] Zhao Yong-shun, Li Xiao-di, Song Shi-ji. Observer-based sliding mode control for stabilization of mismatched disturbance systems with or without time delays. IEEE Trans Syst Man Cybern: Syst 2021;51(12):7337–45.

[19] Hou Qian-kang, Ding Shi-hong, Yu Xing-huo. Composite super-twisting sliding mode control design for PMSM speed regulation problem based on a novel disturbance observer. IEEE Trans Energy Convers 2021;36(4):2591–9.

[20] Hu Jia-bin, Zhang Xue, Zhang Dan, Chen Yun, Ni Hong-jie, Liang Hua-geng. Finite-time adaptive super-twisting sliding mode control for autonomous robotic manipulators with actuator faults. ISA Trans 2024;144:342–51.

[21] Zhao Kai-hui, Jia Ning, Jin-hua She, Wang-ke Dai, Zhou Rui-rui, Liu Wen-chang, Li Xiang-fei. Robust model-free super-twisting sliding-mode control method based on extended sliding-mode disturbance observer for PMSM drive system. Control Eng Pract 2023;139:105657.

[22] Zhang Kang, Wang Li-mei, Fang Xin. High-order fast nonsingular terminal sliding mode control of permanent magnet linear motor based on double disturbance observer. IEEE Trans Ind Appl 2022;58(3):3696–705.

[23] Chu Yun-di, Hou Shi-xi, Wang Cheng, Fei Jun-tao. Recurrent-neural-network-based fractional order sliding mode control for harmonic suppression of power grid. IEEE Trans Ind Inform 2023;19(10):9979–90.

[24] Ok Sangjae, Xu Zhen-yao, Lee Dong-Hee. A sensorless speed control of high-speed BLDC motor using variable slope SMO. IEEE Trans Ind Appl 2024;60(2):3221–8.

[25] Shen Mou-quan, Wang Xian-ming, Park Ju H, Yi Yang, Che Wei-Wei. Extended disturbance-observer-based data-driven control of networked nonlinear systems with event-triggered output. IEEE Trans Syst Man Cybern: Syst 2023;53(5):3129–40.

[26] Krishnaram K, Padmanabhan T Suresh, Alsaif Faisal, Senthilkumar S. Development of grey wolf optimization based modified fast terminal sliding mode controller for three phase interleaved boost converter fed PV system. Sci Rep 2024;14(1):9256.

[27] Shang Yi-lun. Resilient leaderless and leader–follower consensus over random networks through hop communication. Eur J Control 2024;79. Early Access.

[28] Shang Yi-lun. Resilient consensus of switched multi-agent systems. Systems Control Lett 2018;122:12–8.

[29] Liu Gang, Zhang Hai-feng, Song Xin-da. Position-estimation deviation-suppression technology of PMSM combining phase self-compensation SMO and feed-forward PLL. IEEE J Emerg Sel Top Power Electron 2021;9(1):335–44.

[30] Huang Hao, Tu Qun-zhang, Jiang Cheng-ming, Pan Ming. Nonsingular terminal sliding mode control based on sensor-cloud system for permanent magnet in-wheel motor. IEEE Access 2020;8:140399–410.

[31] He Xin-yi, Li Xiao-di, Song Shi-ji. Nonsingular terminal sliding-mode control of second-order systems subject to hybrid disturbances. IEEE Trans Circuits Syst II: Express Briefs 2022;69(12):5019–23.